



# LiNi<sub>0.5</sub>Mn<sub>1.5</sub>O<sub>4</sub> nanoparticles: Synthesis with synergistic effect of polyvinylpyrrolidone and ethylene glycol and performance as cathode of lithium ion battery

H.B. Lin<sup>a</sup>, Y.M. Zhang<sup>a</sup>, J.N. Hu<sup>a</sup>, Y.T. Wang<sup>a</sup>, L.D. Xing<sup>a,b,c</sup>, M.Q. Xu<sup>a,b,c</sup>, X.P. Li<sup>a,b,c</sup>, W.S. Li<sup>a,b,c,\*</sup>

<sup>a</sup> School of Chemistry and Environment, South China Normal University, Guangzhou 510006, China

<sup>b</sup> Key Laboratory of Electrochemical Technology on Energy Storage and Power Generation of Guangdong Higher Education Institutes, South China Normal University, Guangzhou 510006, China

<sup>c</sup> Engineering Research Center of Materials and Technology for Electrochemical Energy Storage (Ministry of Education), South China Normal University, Guangzhou 510006, China

## HIGHLIGHTS

- LiNi<sub>0.5</sub>Mn<sub>1.5</sub>O<sub>4</sub> nanoparticles are synthesized with synergistic effect of PVP and EG.
- The LiNi<sub>0.5</sub>Mn<sub>1.5</sub>O<sub>4</sub> nanoparticles exhibit excellent rate capability and cyclic stability.
- Charging protocol of CC followed by CV step helps understand the excellent performance.

## ARTICLE INFO

### Article history:

Received 22 November 2013

Received in revised form

10 January 2014

Accepted 20 January 2014

Available online 30 January 2014

### Keywords:

LiNi<sub>0.5</sub>Mn<sub>1.5</sub>O<sub>4</sub>

Jahn–Teller distortion

Nanoparticle

Lithium battery

## ABSTRACT

LiNi<sub>0.5</sub>Mn<sub>1.5</sub>O<sub>4</sub> was synthesized by sol–gel using polyvinylpyrrolidone (PVP) as dispersant and ethylene glycol (EG) as size-controlled additive. Crystal structure, particle morphology and electrochemical performance of the resulting product (PVP–LNMO) as cathode of lithium ion battery were investigated with XRD, SEM, CV, EIS, and charge/discharge test, with a comparison of LiNi<sub>0.5</sub>Mn<sub>1.5</sub>O<sub>4</sub> (LNMO) synthesized under the same conditions but without using PVP and EG. It is found that PVP–LNMO is composed of dispersed LiNi<sub>0.5</sub>Mn<sub>1.5</sub>O<sub>4</sub> nanoparticles with uniform size, and exhibits far better rate capability and cyclic stability than LNMO. The particles of the latter are in micro size due to the aggregation of smaller primary particles. PVP–LNMO delivers a reversible discharge capacity of 96 mAh g<sup>−1</sup> at 20C rate with a capacity retention of 93% at 5C rate after 500 cycles, while only 40 mAh g<sup>−1</sup> and 53% for LNMO, respectively. The nanoparticles provide shorter distance for electron and lithium ion transport and larger surface area for electron exchange on the electrode/electrolyte interface, resulting in the far better rate capability of PVP–LNMO than LNMO, while the room among nanoparticles in PVP–LNMO releases the stress of Jahn–Teller distortion that causes destruction of LNMO microparticles, resulting in the excellent cyclic stability.

© 2014 Elsevier B.V. All rights reserved.

## 1. Introduction

Lithium ion battery has been widely used in electronic devices such as cell phones, digital cameras and laptop, owing to its high energy density and excellent cycling performance, but its energy density needs to be improved for the large-scale applications such

as power source in electric vehicles [1]. Spinel-structured LiNi<sub>0.5</sub>Mn<sub>1.5</sub>O<sub>4</sub> (LNMO) is a promising cathode material for energy density improvement of current lithium ion battery, because it provides higher working voltage (4.75 V) than commercial cathodes such as LiFePO<sub>4</sub> (3.4 V), LiCoO<sub>2</sub> (3.9 V) and LiMn<sub>2</sub>O<sub>4</sub> (4.1 V) [2].

However, LNMO presents poor cyclic performance due to the dissolution of Mn<sup>2+</sup>, resulting from the disproportionation reaction of Mn<sup>3+</sup>, and the particle separation resulting from Jahn–Teller distortion during charge and discharge cycles, especially at elevated temperature [3,4]. Doping Cr, Co, Ru, Ti, Nb, Mo or Mg in LNMO [5–12] and coating LNMO with metal oxides [13–16] are the main

\* Corresponding author. School of Chemistry and Environment, South China Normal University, Guangzhou 510006, China. Tel./fax: +86 20 39310256.

E-mail address: [liwsh@scnu.edu.cn](mailto:liwsh@scnu.edu.cn) (W.S. Li).

approaches for the stability improvement of LNMO, but the improvement is not satisfying and at the expense of a capacity loss.

Nanoparticles of LNMO exhibits improved performances in terms of rate capability and cyclic stability [17,18]. Nanoparticles provide short paths for lithium ion transportation in particles and thus enhance rate capability of LNMO. On the other hand, the room among nanoparticles accommodates the lattice stress caused by Jahn–Teller distortion during cycles and thus enhances the cyclic stability of LNMO.

The performance of spinel LNMO depends to a great extent on the sintering temperature [19]. It was reported that the spinel

LNMO sintered under 800 °C exhibited well cyclic stability [20]. Polyvinylpyrrolidone (PVP) was used to control particle size of LNMO [21], which is similar to the sucrose-assisted combustion method [22]. However, when the sintering temperature is over 800 °C, the nanoparticles aggregates resulting in the deteriorated performance of LNMO [23].

In this work, we proposed a facile method to synthesize LNMO nanoparticles, in which chemical homogeneity on an atomic scale was assured and nanosize particles were obtained at 800 °C with the synergistic effect of ethylene glycol (EG) as size-controller and PVP as dispersants. The performance of the resulting LNMP

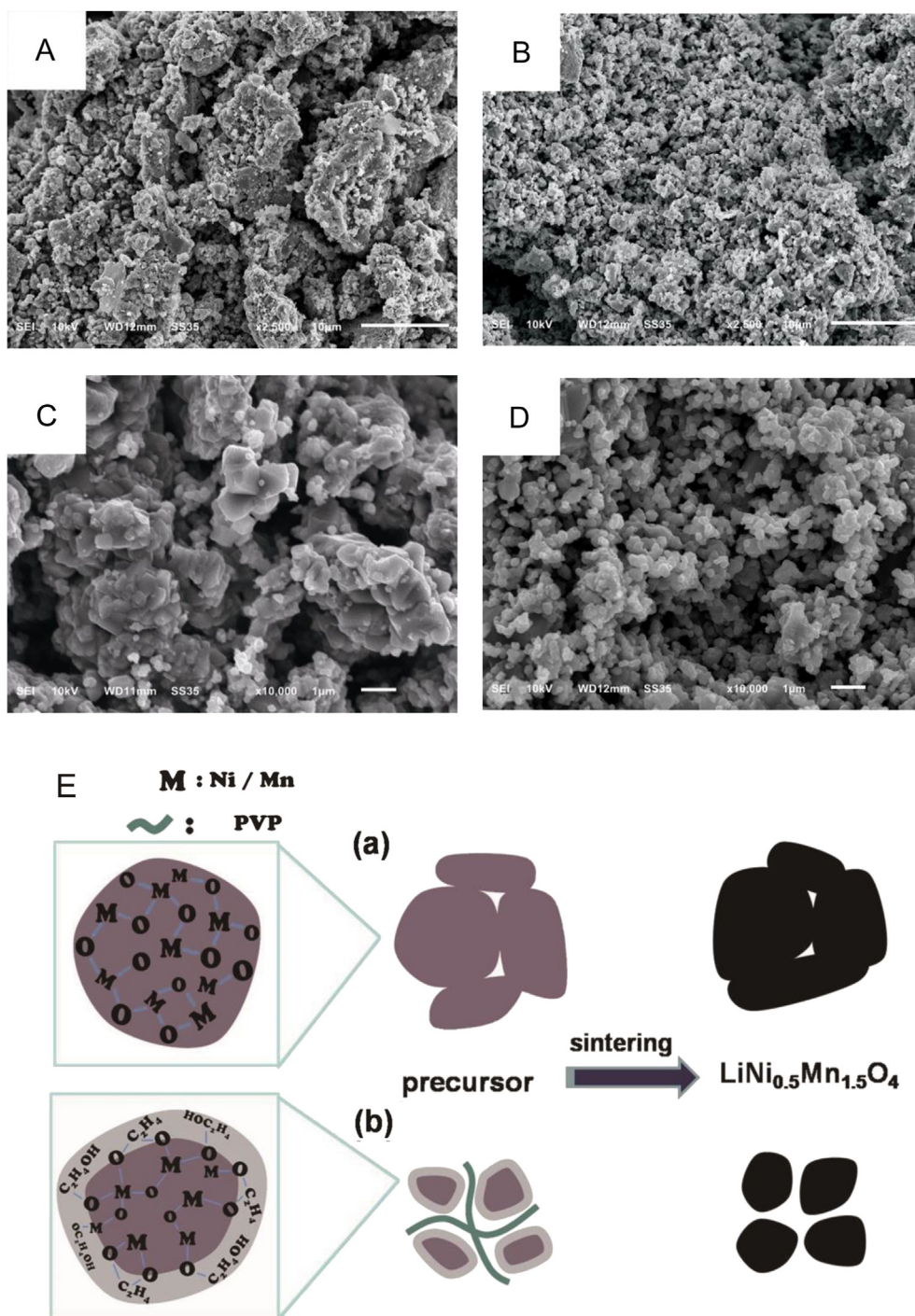


**Fig. 1.** SEM images of LNMO (A and C) and PVP–LNMO (B and D) and schematic formation mechanism of samples (E, a: LNMO and b: PVP–LNMO).

nanoparticles (marked as PVP–LNMP) was compared with that of the LNMO microparticles synthesized without using EG and PVP (marked as LNMP).

## 2. Experimental

### 2.1. Preparation

Typically, 0.5 g PVP was dispersed in the mixed solvent of 50 mL distilled water and 2 mL ethylene glycol. Subsequently, manganese acetate ( $\text{Mn}(\text{CH}_3\text{COO})_2 \cdot 4\text{H}_2\text{O}$ ), nickel acetate ( $\text{Ni}(\text{CH}_3\text{COO})_2 \cdot 4\text{H}_2\text{O}$ ) and lithium acetate ( $\text{LiCH}_3\text{COO} \cdot 2\text{H}_2\text{O}$ ) in a stoichiometric amount were added. The solution was heated to 90 °C under constant magnetic stirring. The water in the multi-component system was evaporated to achieve a green viscous precursor, which was then dried at 120 °C under vacuum and further calcined at 800 °C under air atmosphere for 10 h to obtain the final product. LNMO with micro size particles for comparison was prepared in the same way without using EG or PVP. The resulting samples were heated and cooled at a rate of 5 °C min<sup>−1</sup>. All chemicals for the sample preparation were purchased from Aladin (Wuhan, China) and used without further treatment.

### 2.2. Characterization

The morphology of LNMO was observed by scanning electron microscope (JSM-6380, Japan). The surface area was determined with BET (Micromeritics ASAP 2020 M) at liquid nitrogen temperature (77 K). The crystal structures of the samples were analyzed by X-ray diffraction (BRUKER D8 ADVANCE, Germany) with Cu K<sub>α</sub> radiation.

### 2.3. Electrochemical measurements

The electrode was prepared by mixing 75 wt% active material with 15 wt% acetylene black and 10 wt% polyvinylidene difluoride (PVDF) binder, coating the mixture on an aluminum sheet, and then cutting the sheet into pieces with 1 cm × 1 cm. The active material loading in the composite electrode was 2–3 mg cm<sup>−2</sup>. The CR2025 coin cell was assembled in an Ar-filled MBraun glove box by using prepared electrode as cathode, lithium film as anode, Celgard 2400 as separator and 1 M LiPF<sub>6</sub> in EC:DMC (1:2 in volume) as electrolyte.

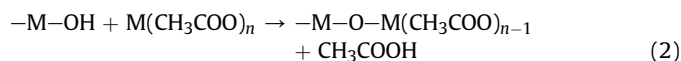
Charge/discharge test was performed on Land cell test system (Land CT2001A, China). Cells were cycled between 3.5 and 4.95 V (vs. Li/Li<sup>+</sup>) at 25 °C with a charging protocol of constant current (CC) followed by a constant voltage (CV) step at 4.95 V (vs. Li/Li<sup>+</sup>) till the current decreased to one tenth of the CC (1C = 147 mA g<sup>−1</sup>). The cyclic voltammetry was performed on Solartron-1470E CellTest at 25 °C between 3.5 V and 4.95 V at a sweep rate of 0.1 mV s<sup>−1</sup>. The AC impedance of the cells was measured on Autolab (PGSTAT302N) over the frequency range of 10<sup>5</sup> Hz to 0.01 Hz with an amplitude of 5 mV<sub>rms</sub>.

## 3. Results and discussion

### 3.1. Crystal structure and morphology

Fig. 1 presents the typical morphology and particle size of the resulting samples, showing the difference between two samples. The sample LNMP consists of the secondary particles (about 10 μm) formed from the aggregation of the primary particles (0.5–1 μm), as shown in Fig. 1A and C. Differently, the sample PVP–LNMO consists of nanoparticles (~200 nm) that are dispersed separately, as shown in Fig. 1B and D.

Sol–gel synthesis of oxide materials, a route leading to chemical homogeneity on an atomic scale in a multi-component system, has been widely used in the preparation of electrode materials including LNMO [24–26]. The sol–gel synthesis is a multi-process which involves conversion of a precursor solution into a sol and subsequently transition of the gel to an oxide compound. A gel with a continuous inorganic network is produced by a series of chemical reactions including the hydrolysis, polymerization and condensation [27]. In this work, acetates were used as organometallic compounds for forming the gel. On addition of water, the acetate  $\text{M}(\text{CH}_3\text{COO})_n$  (M = Mn, Ni and Li) hydrolyzes to form the hydroxide  $\text{M}(\text{OH})_n$ , followed by polymerization forming the –M–O–M– bonds as described in Eqs. (1) and (2):



In this manner, inorganic polymeric oxide networks are built up. The condensation of the polymeric oxide forms nanoparticles progressively. The nanoparticle is inhomogeneous in size and easily aggregated during the condensation in the case without using EG and PVP, while the growth and aggregation of the particle are restricted and dispersed LNMO nanoparticles with uniform size can be obtained with synergistic effect of EG and PVP, as illustrated in Fig. 1E. Ethylene glycol, a molecule with hydroxyl, takes part in the formation of sol and restricts the growth of particles [28]. As a non-ionic surfactant, PVP forms micelle in aqueous solution and disperses the particles [28,29]. Surfactants are well known to effectively tailor particle shape and size in the synthetic process [29,30]. The BET specific surface area measurement confirms the smaller size and the more uniform dispersion of PVP–LNMO particles. PVP–LNMO has a specific surface of 3.76 m<sup>2</sup> g<sup>−1</sup>, while LNMO has only 0.88 m<sup>2</sup> g<sup>−1</sup>.

X-ray diffraction shows that both LNMO and PVP–LNMO exhibit cubic spinel structure (the space group Fd-3m), as shown in Fig. 2. The lattice parameters calculated from XRD using Rietveld refinement are 8.166 Å for LNMO and 8.168 Å for PVP–LNMO, which are almost the same. This result indicates that the use of EG and PVP does not affect the crystal structure of the resulting product. It can be seen from Fig. 2 that both samples have weak diffraction peaks at

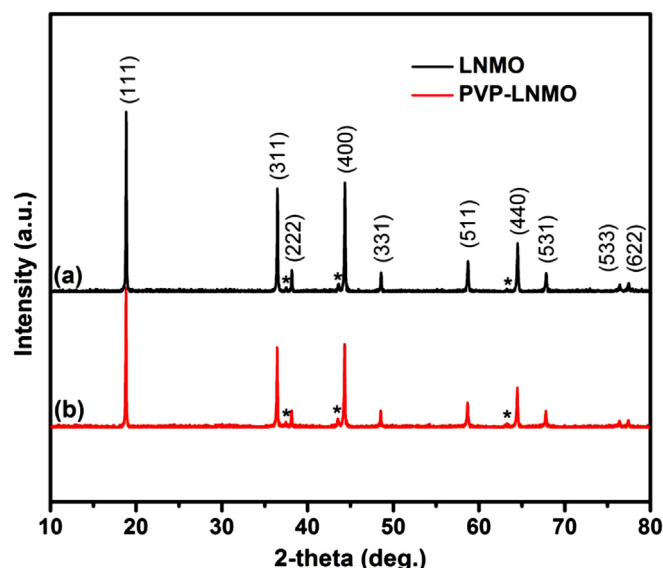


Fig. 2. X-ray diffraction patterns of LNMO (a) and PVP–LNMO (b).

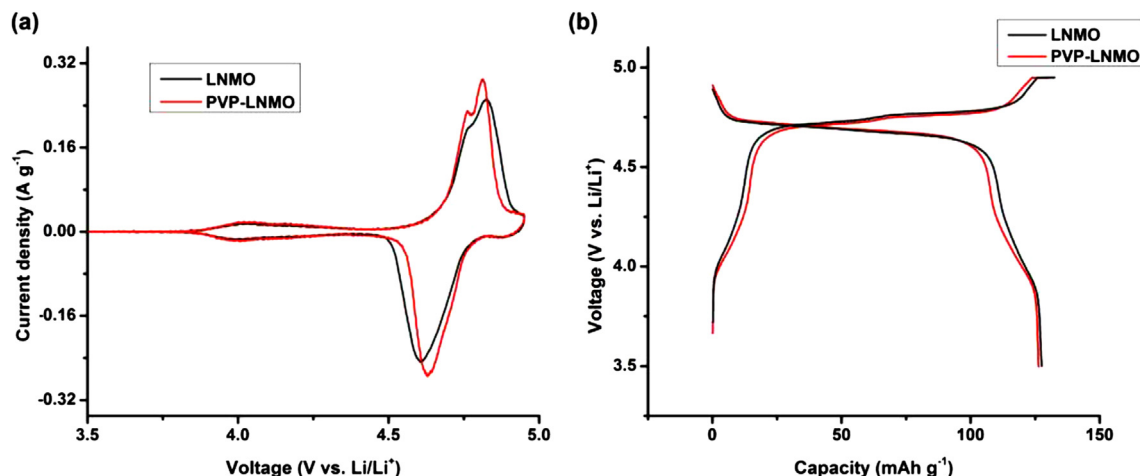


Fig. 3. Cyclic voltammogram at a scan rate of  $0.1 \text{ mV s}^{-1}$  (a) and typical charge–discharge profile of LNMO and PVP–LNMO electrodes at  $0.5\text{C}$  between  $3.5$  and  $4.95 \text{ V}$  (b).

$37.91$ ,  $43.86$  and  $63.5 \text{ } 2\theta$ , as marked with asterisks, which can be ascribed to  $\text{NiO}$  and  $\text{Li}_x\text{Ni}_y\text{O}$ . It is a common feature that such impurities are observed in the synthesis of  $\text{LiNi}_{0.5}\text{Mn}_{1.5}\text{O}_4$ , when the Ni content  $x$  in  $\text{LiNi}_x\text{Mn}_{2-x}\text{O}_4$  exceeds  $0.2$  [31].

### 3.2. Electrochemical performance

The spinel structure of the resulting samples was confirmed with cyclic voltammetry at low scan rate and constant current

charge/discharge test at small current rate. Fig. 3 presents the cyclic voltammograms and charge/discharge profiles of the resulting samples, which indicates that both samples are characteristic of spinel structure. The redox peaks and the potential plateau at about  $4.7 \text{ V}$  in the cyclic voltammograms (Fig. 3a) and the charge/discharge profile (Fig. 3b) are ascribed to the two-step oxidation/reduction of  $\text{Ni}^{2+}/\text{Ni}^{3+}$  and  $\text{Ni}^{3+}/\text{Ni}^{4+}$ , while the small redox peaks and the short potential plateau at about  $4.0 \text{ V}$  are attributed to the redox reaction of  $\text{Mn}^{3+}/\text{Mn}^{4+}$  couples [11,32]. Apparently, the redox

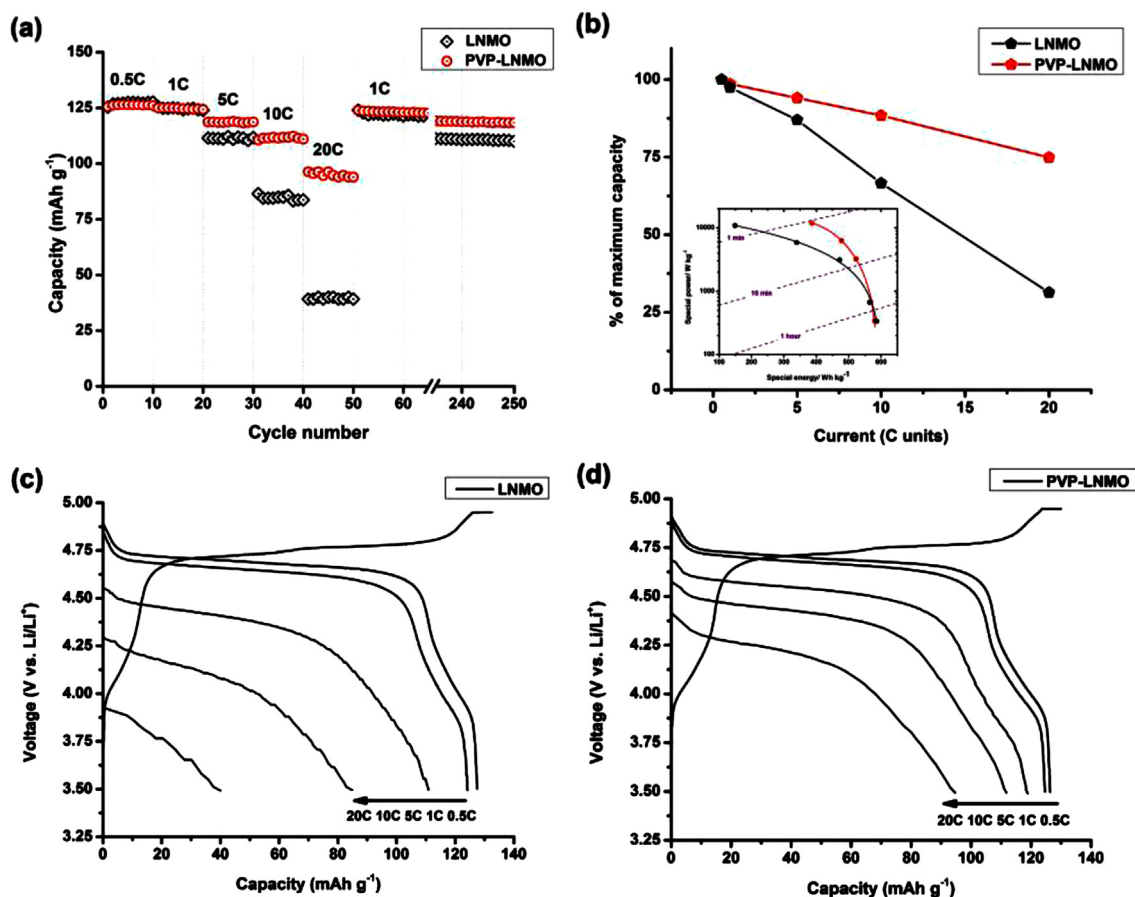


Fig. 4. Specific capacity as a function of cycle number at different current rates (a), normalized discharge capacity values and Ragone plot (b), and discharge voltage–capacity profiles for LNMO (c) and PVP–LNMO (d).



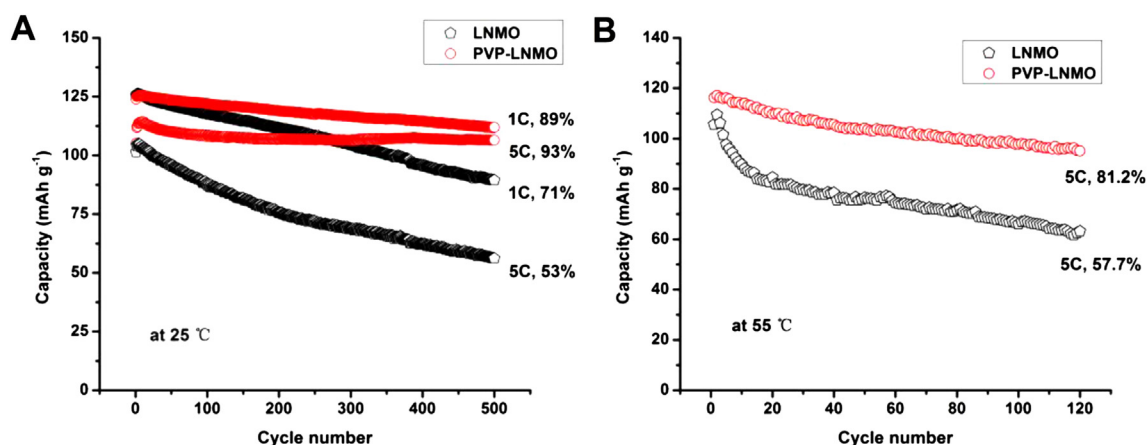


Fig. 5. Cyclic performance of LNMO and PVP-LNMO electrodes (A) at 25 °C and (B) at 55 °C. The cells are charged/discharged at 1C and 5C rate (1C = 147 mA g<sup>-1</sup>).

of nickel ions mainly contributes to the lithium ion insertion/extraction capacity of spinel lithium nickel manganese oxide. Although both samples have similar cyclic voltammetric behavior and charge/discharge profile, some differences can be distinguished between two samples: the difference in redox peak potentials of nickel ions is smaller for PVP-LNMO (ca. 0.13 V) than LNMO (ca. 0.16 V). This difference indicates that PVP-LNMO has faster lithium insertion/extraction kinetics (less polarization during lithium insertion/extraction process), which confirms the nanosize particles of PVP-LNMO. It can be expected that the difference in polarization between two samples will become significant when increasing charge/discharge rate.

Fig. 4 compares the rate capability of two samples. Fig. 4a presents the variation of discharge capacity with current rates. The cells were charged at 0.5C (1C = 147 mA g<sup>-1</sup>) and discharged at different rates. The capacity delivered by the two samples is almost the same at low rates. However, the significant difference in rate capability is observed at 5C rate and the difference increases as the rate current increases further. Both samples deliver a discharge capacity of 125 mAh g<sup>-1</sup> at 1C. At 20C, however, PVP-LNMO delivers a discharge capacity of 96 mAh g<sup>-1</sup> compared to the 40 mAh g<sup>-1</sup> of LNMO.

Fig. 4b presents the normalized discharge capacity on the base of 0.5 C, which indicates iconically the difference in rate capability between two samples. PVP-LNMO retains 75% of its 0.5 C initial discharge capacity at 20 C, while only 31% for LNMO. The inset of Fig. 4b compares the specific power and energy of two samples at different rates. The specific power ( $P$ ) was calculated according to  $P = Wt^{-1}$ , where  $W$  is the specific energy calculated by integrating the discharging curves and  $t$  is the total discharging time. As the specific power increases from 340 W kg<sup>-1</sup> to 12,000 W kg<sup>-1</sup>, the specific energy of LNMO changes from 586 Wh kg<sup>-1</sup> to 149 Wh kg<sup>-1</sup>, while PVP-LNMO only from 581 Wh kg<sup>-1</sup> to 386 Wh kg<sup>-1</sup>. The excellent rate capability of PVP-LNMO should be attributed to its nanosized and well dispersed particles. The nanoparticle provides the short transport distances for both lithium-ion and electron transport within the particles as well as a large electrode/electrolyte contact area [6,33,34].

Fig. 4c and d presents the discharge profiles of two samples at different rates. The increase of the rate results in the overlap of two plateaus in the 4.75 V and 4 V and the negative shift of discharge potential. These changes are less significant for PVP-LNMO than LNMO, confirming that PVP-LNMO has smaller polarization than LNMO during lithium insertion/extraction process.

Table 1

Comparison of the electrochemical performance property of PVP-LNMO with samples reported in literature.

Reference	Additives	Cathode composition (wt.%)	Rate capability		Cyclic stability (25 °C)		
			$I_{\max}$ (C units)	Capacity at $I_{\max}$ (mAh g <sup>-1</sup> )	$I$ (C units)	Cycle number	Capacity retention (%)
[25]	Ethylene glycol	80 wt.% LNMO 10 wt.% carbon black 10 wt.% PVDF	5	117	5	50	95.7
[33]	Resorcinol formaldehyde	76 wt.% LNMO 12 wt.% Super S carbon 12 wt.% PVDF	40	90	1	200	93.7
[26]	PVP	80 wt.% LNMO 10 wt.% carbon black 10 wt.% PVDF	15	103	1	200	93.9
[35]	Triblock copolymer F127	70 wt.% LNMO 20 wt.% acetylene black 10 wt.% PVDF	50	96	1	500	86
[23]	PEG 400	70 wt.% LNMO 20 wt.% acetylene black 10 wt.% PVDF	15	60	0.25	100	78
This work	PVP and ethylene glycol	75 wt.% LNMO 15 wt.% acetylene black 10 wt.% PVDF	20	96	5	500	93

Nanoparticles of battery materials provides larger specific surface area for electron transfer reaction and thus exhibits better rate capability than larger particles. However, increased surface area of nanoparticles leads usually to poor cycle stability of battery materials due to the dissolution of materials in electrolyte. It can be noted from Fig. 4a that PVP–LNMO recovers its primary 1 C discharge capacity after cycling at 20 C and has a higher discharge capacity retention than LNMO after 200 cycles. The discharge capacity at 200th cycle is  $119 \text{ mAh g}^{-1}$  for PVP–LNMO but only  $110 \text{ mAh g}^{-1}$ . This result suggests that PVP–LNMO exhibit not only better rate stability and but also cycle stability than.

To confirm the cycle stability of PVP–LNMO, the long-life cycling performance of PVP–LNMO and LNMO was compared at 1C and 5C charge/discharge rate (Fig. 5). Fig. 5A presents the discharge variations of two sample at 1C and 5 C during 500 cycles at  $25^\circ\text{C}$ . After 500 cycles, the capacity retentions are 89% at 1C and 93% at 5C for PVP–LNMO, while only 71% at 1C and 53% at 5C for LNMO,

indicating that PVP–LNMO exhibits excellent cycle stability, especially at high rate. To our knowledge, this may be one of the best performances of long-life cycles of  $\text{LiNi}_{0.5}\text{Mn}_{1.5}\text{O}_4$  samples that have been reported. The best capacity retentions reported in references are 86% at 1C rate after 500 cycles [35], 90.5% at 1C and 92.5% at 5C after 400 cycles [36] and 91% at 2C and 83% at 5C after 500 cycles [37], as shown in Table 1. Under elevated temperature, the difference between two samples becomes more significant, as shown in Fig. 5B.

In order to understand why PVP–LNMO exhibits excellent cycle stability, the charge performance of two samples was analyzed by separating charge capacity into constant current (CC) and constant voltage (CV) parts, and the cycled electrodes were characterized with cyclic voltammetry, EIS, XRD, and SEM. Cyclic voltammetry and EIS were performed on the cells charged and discharged at 1C in a voltage range of 3.5–4.95 V for three cycles firstly. The scan rate was  $0.1 \text{ mV s}^{-1}$  in cyclic voltammetry and the voltage was kept at

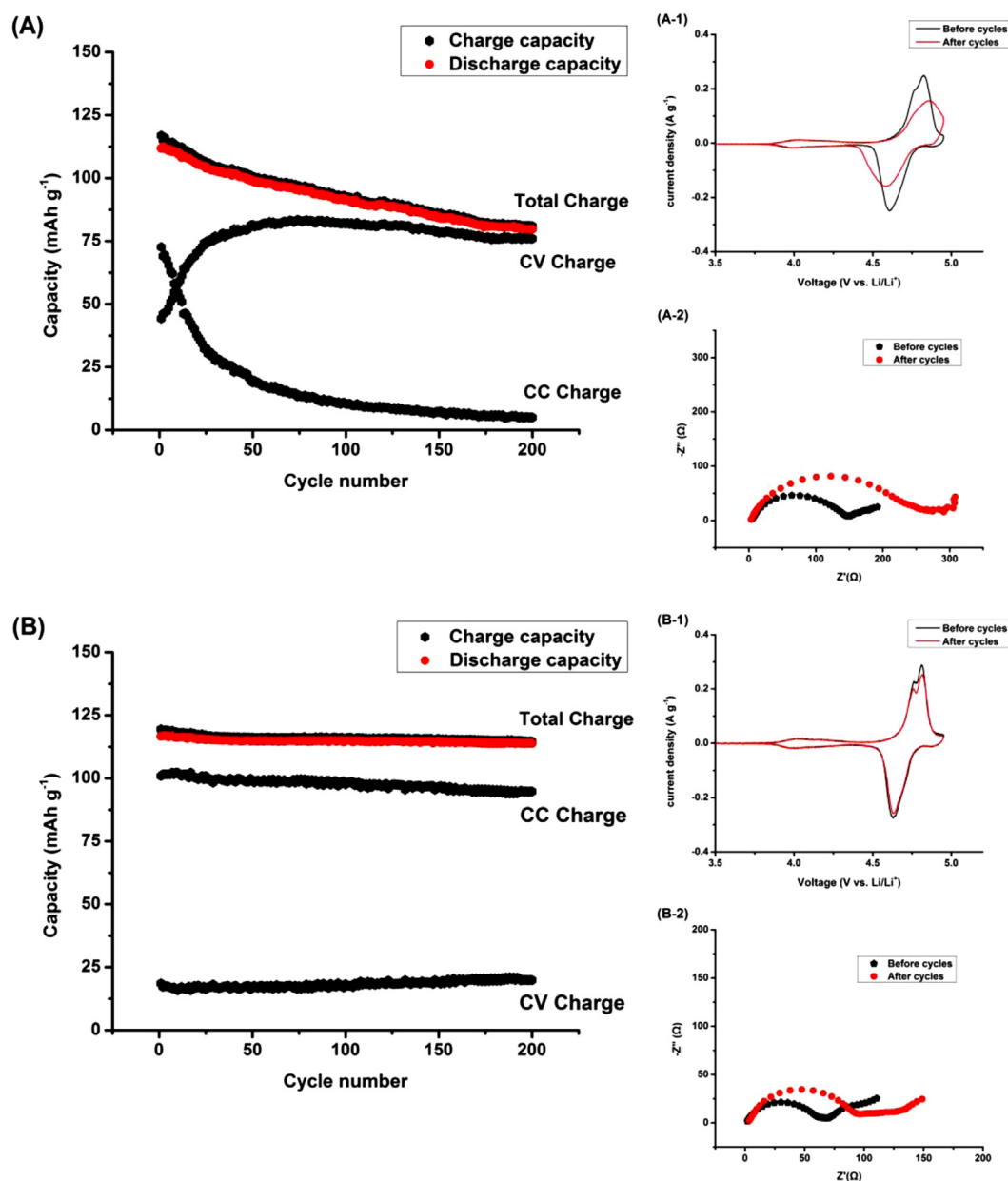


Fig. 6. Charge capacity separation of LNMO (A) and PVP–LNMO (B) in terms of constant current (CC) and voltage (CV) at 5C and corresponding CV and EIS before and after cycling.

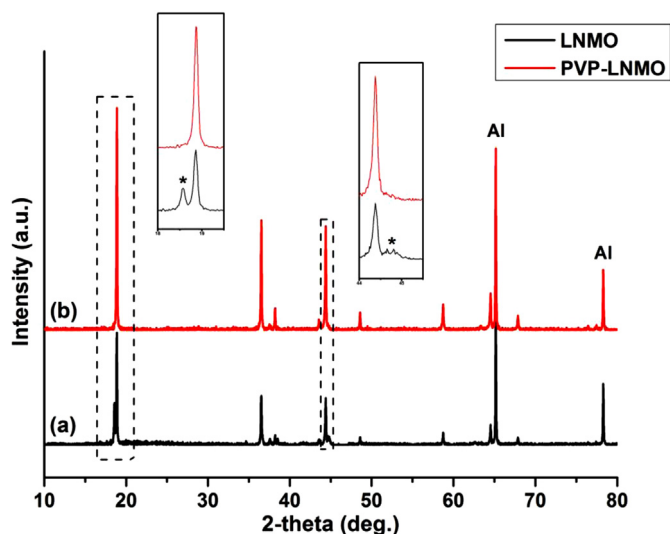


Fig. 7. XRD patterns of LNMO (a) and PVP–LNMO electrodes after 200 cycles.

4.75 V in the EIS measurement. Then the cells experienced 200 cycles between 3.5 and 4.95 V at 25 °C, with a charging protocol of CC followed by CV till the current decreased to one tenth of CC ( $1C = 147 \text{ mA g}^{-1}$ ). The charge and discharge currents are 5C. Cyclic voltammetry and EIS were also performed on the electrodes cycled for 200 cycles. At last, the cycled electrodes were examined with XRD and SEM.

Usually, CV charge to battery materials can recover the capacity loss of CC charge in the charging protocol of CC followed by CV, especially at high rate CC charge [30]. The recovery capacity reflects the rate-accepted ability and the stability of the battery materials. Fig. 6A and B presents the variation of charge and discharge capacities, together with the separated CC and CV charge capacities, of PVP–LNMO and LNMO with cycling. It can be seen that two

samples exhibit different variation of CC and CV charge capacities. LNMO has an initial CV charge capacity of ca.  $43 \text{ mAh g}^{-1}$  and its CV charge capacity increases significantly with cycling, as shown in Fig. 6A. Differently, PVP–LNMO has a lower initial CV charge capacity (ca.  $15 \text{ mAh g}^{-1}$ ) and its CV charge capacity increase slightly even after 200 cycles, as shown in Fig. 6B. In other words, the CC charge of PVP–LNMO accounts mainly for charge capacity but the CC charge of LNMO takes up only a small part of the total charge capacity and needs to be compensated by CV charge. This analysis demonstrates that PVP–LNMO has far better rate-accepted ability and structure stability than LNMO.

The nanoparticles in PVP–LNMO not only exhibits rate capability by providing short distances for Li ion and electron transport and large specific surface area for electron exchange, but also keeps its structure stability by providing room among particles for the relief of the lattice stress caused by Jahn–Teller distortion due to the formation of  $\text{Mn}^{3+}$  during cycles [6,34,38]. In the fully lithiated LNMO, the average oxidation state of Mn in LNMO is equal to 4. However, after discharged, especially at the voltage lower than 4.0 V,  $\text{Mn}^{3+}$  is formed [3]. In contrast, the larger particles in LNMO not only yields poor rate capability due to the larger resistance for electron transfer on the interface and lithium ion transport in the bulk [39], but also leads more easily to structure destruction and primary particle separation due to the Jahn–Teller distortion. In addition, the CV charge for longer time to the larger particles at the voltage as high as 4.95 V increases the decomposition of electrolyte and the dissolution of LNMO [40].

The faster kinetics of lithium ion insertion/extraction and better stability of structure in PVP–LNMO can be also demonstrated by cyclic voltammetry and EIS. After 200 cycles, the cyclic voltammogram of PVP–LNMO almost keeps the same shape as its initial one (Fig. 6B1). However, the cyclic voltammogram of LNMO changes significantly: the redox peak current was reduced and the difference in peak potentials becomes wider (Fig. 6A1), implying that the LNMO electrode suffering serious polarization and the some structure might happen in the electrode due to the cycling.

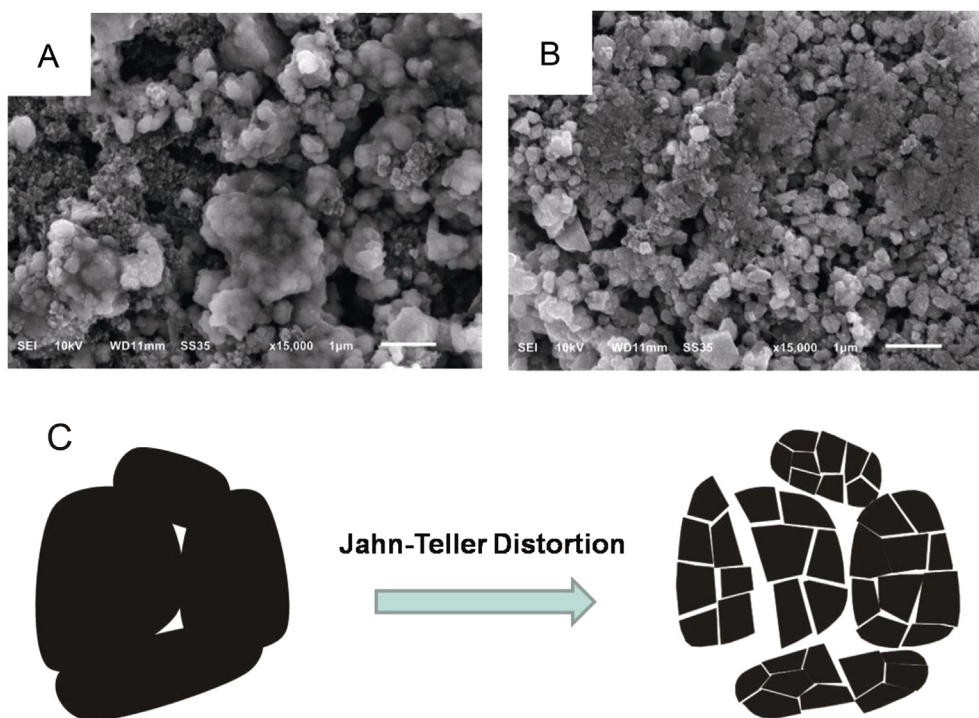


Fig. 8. SEM images of LNMO (A) and PVP–LNMO (B) electrodes after 200 cycles and schematic separation of particles suffered from the Jahn–Teller distortion of LNMO particles (C).

The interfacial resistance (taken from the semicircle impedance of the impedance spectra [41,42]) changes slightly for PVP–LNMO, from 60  $\Omega$  to 80  $\Omega$  (Fig. 6B2), while significantly for LNMO, from 120  $\Omega$  to 260  $\Omega$  (Fig. 6A2), indicative of the faster kinetics of lithium ion insertion/extraction in PVP–LNMO than in LNMO.

The structure change appearing in the cycled LNMO electrode was confirmed by XRD and SEM examination. Fig. 7 presents the XRD patterns of PVP–LNMO and LNMO taken from the cycled electrodes after 200 cycles. Both samples retain their spinel structure. However, it can be found by comparing Fig. 7 with Fig. 2 that the difference in peak intensities between PVP–LNMO and LNMO have changed after cycling: LNMO has more intensive diffraction peaks before cycling (Fig. 2) but the corresponding peaks become less intensive after cycling compared to those of PVP–LNMO (Fig. 7). In addition, there appear some other diffraction peaks (as marked with asterisks in the inset of Fig. 7) in the XRD pattern of cycled LNMO electrode. These results suggest that the crystal particles of LNMO have been changed significantly and some  $\text{LiNi}_{0.5}\text{Mn}_{1.5}\text{O}_4$  have decomposed due to the cycling, while PVP–LNMO remains its structure stability.

Fig. 8 presents the SEM images of the cycled electrodes for 200 cycles. It can be found by comparing Fig. 8B with Fig. 2D that the morphology and particle size of PVP–LNMO remain almost the same after cycling, except for the additives used in the electrodes. As shown in Fig. 8A, however, the microparticles, consisting of smaller primary particles, in the pristine LNMO (Fig. 2C) have been separated into nanoparticles that are smaller than the primary particles. These results verify that the particle morphology remain stable in PVP–LNMO but deteriorates in LNMO. In the case of LNMO, the stress resulting from Jahn–Teller distortion during cycles leads to the separation and even destruction of the primary particles (as shown in Fig. 8C). The separated particles loss their electronic contact, resulting in the poor cyclic stability of LNMO. On the other hand, the destruction of particles in LNMO is accompanied with the decomposition of  $\text{LiNi}_{0.5}\text{Mn}_{1.5}\text{O}_4$ . In the case of PVP–LNMO, the room among nanoparticles releases the stress of Jahn–Teller distortion during cycles and the morphology and crystal structure remain stable after cycling, resulting in the excellent cyclic stability.

#### 4. Conclusions

In this paper, we reported a novel sol–gel method for synthesizing  $\text{LiNi}_{0.5}\text{Mn}_{1.5}\text{O}_4$  nanoparticles, in which polyvinylpyrrolidone (PVP) was used as dispersant and ethylene glycol (EG) as size-controlled additive. With the synergic effect of PVP and EG, dispersed  $\text{LiNi}_{0.5}\text{Mn}_{1.5}\text{O}_4$  nanoparticles with uniform size can be obtained. The resulting product (PVP–LNMO) exhibits excellent rate capability and cyclic stability, compared to the  $\text{LiNi}_{0.5}\text{Mn}_{1.5}\text{O}_4$  product (LNMO) synthesized under the same conditions but without using PVP and EG, whose particles formed by the aggregation of smaller primary particles are in micro size. The nanoparticles provide shorter distance for electron and lithium ion transport and larger surface area for electron exchange on the electrode/electrolyte interface, resulting in the far better rate capability of PVP–LNMO than LNMO. On the other hand, the room among nanoparticles in PVP–LNMO can releases the stress of Jahn–Teller distortion during cycles that causes destruction of LNMO microparticles, resulting in its excellent cyclic stability. The PVP–LNMO prepared this work exhibits good performance compared to the samples reported in literature.

#### Acknowledgments

This work is financially supported from the joint project of National Natural Science Foundation of China and Natural Science

Foundation of Guangdong Province (Grant No. U1134002), the National Natural Science Foundation (Grant No. 21273084), the Natural Science Fund of Guangdong Province (Grant No. 10351063101000001), and the Key Project of Science and Technology in Guangdong Province (Grant No. 2012A010702003).

#### References

- [1] T.-H. Kim, J.-S. Park, S.K. Chang, S. Choi, J.H. Ryu, H.-K. Song, *Adv. Energy Mater.* 2 (2012) 860–872.
- [2] A. Kraytsberg, Y. Ein-Eli, *Adv. Energy Mater.* 2 (2012) 922–939.
- [3] B. Li, L. Xing, M. Xu, H. Lin, W. Li, *Electrochim. Commun.* 34 (2013) 48–51.
- [4] T. Yoon, S. Park, J. Mun, J.H. Ryu, W. Choi, Y.-S. Kang, J.-H. Park, S.M. Oh, *J. Power Sources* 215 (2012) 312–316.
- [5] M. Akklouch, J.M. Amarilla, R.M. Rojas, I. Saadoun, J.M. Rojo, *J. Power Sources* 185 (2008) 501–511.
- [6] M. Akklouch, J.M. Amarilla, I. Saadoun, J.M. Rojo, *J. Power Sources* 196 (2011) 10222–10227.
- [7] U. Lafont, C. Locati, W.J.H. Borghols, A. Łasińska, J. Dygas, A.V. Chadwick, E.M. Kelder, *J. Power Sources* 189 (2009) 179–184.
- [8] M.-W. Jang, H.-G. Jung, B. Scrosati, Y.-K. Sun, *J. Power Sources* 220 (2012) 354–359.
- [9] H. Wang, T.A. Tan, P. Yang, M.O. Lai, L. Lu, *J. Phys. Chem. C* 115 (2011) 6102–6110.
- [10] T.-F. Yi, B. Chen, Y.-R. Zhu, X.-Y. Li, R.-S. Zhu, *J. Power Sources* 247 (2014) 778–785.
- [11] T.-F. Yi, Y. Xie, Y.-R. Zhu, R.-S. Zhu, M.-F. Ye, *J. Power Sources* 211 (2012) 59–65.
- [12] J.H. Kim, S.T. Myung, C.S. Yoon, I.H. Oh, Y.K. Sun, *J. Electrochem. Soc.* 151 (2004) A1911.
- [13] J.-H. Cho, J.-H. Park, M.-H. Lee, H.-K. Song, S.-Y. Lee, *Energy Environ. Sci.* 5 (2012) 7124–7131.
- [14] J.C. Arrebola, A. Caballero, L. Hernan, J. Morales, *J. Power Sources* 195 (2010) 4278–4284.
- [15] G. Zhao, Y. Lin, T. Zhou, Y. Lin, Y. Huang, Z. Huang, *J. Power Sources* 215 (2012) 63–68.
- [16] D. Liu, J. Trottier, P. Charest, J. Fr chet, A. Guerfi, A. Mauger, C.M. Julien, K. Zaghib, *J. Power Sources* 204 (2012) 127–132.
- [17] L. Zhou, D. Zhao, X. Lou, *Angew. Chem. Int. Ed. Engl.* 51 (2012) 239–241.
- [18] X. Zhang, F. Cheng, J. Yang, J. Chen, *Nano Lett.* (2013).
- [19] M. Kunduraci, J.F. Al-Sharab, G.G. Amatucci, *Chem. Mater.* 18 (2006) 3585–3592.
- [20] Y. Dong, Z. Wang, H. Qin, X. Sui, *RSC Adv.* 2 (2012) 11988.
- [21] M.V. Reddy, H.Y. Cheng, J.H. Tham, C.Y. Yuan, H.L. Goh, B.V.R. Chowdari, *Electrochim. Acta* 62 (2012) 269–275.
- [22] J.M. Amarilla, R.M. Rojas, F. Pico, L. Pascual, K. Petrov, D. Kovacheva, M.G. Lazarraga, I. Lejona, J.M. Rojo, *J. Power Sources* 174 (2007) 1212–1217.
- [23] J.C. Arrebola, A. Caballero, M. Cruz, L. Hernan, J. Morales, E.R. Castellon, *Adv. Funct. Mater.* 16 (2006) 1904–1912.
- [24] A. Bhaskar, N.N. Bramnik, D.M. Trots, H. Fuess, H. Ehrenberg, *J. Power Sources* 217 (2012) 464–469.
- [25] X. Zhang, J. Liu, H. Yu, G. Yang, J. Wang, Z. Yu, H. Xie, R. Wang, *Electrochim. Acta* 55 (2010) 2414–2417.
- [26] J. Mao, K. Dai, Y. Zhai, *Electrochim. Acta* 63 (2012) 381–390.
- [27] B.B. Lakshmi, C.J. Patrissi, C.R. Martin, *Chem. Mater.* 9 (1997) 2544–2550.
- [28] X. Xiang, X. Li, W. Li, *J. Power Sources* 230 (2013) 89–95.
- [29] X. Zhang, F. Cheng, K. Zhang, Y. Liang, S. Yang, J. Liang, J. Chen, *RSC Adv.* 2 (2012) 5669–5675.
- [30] Z. Yan, S. Cai, X. Zhou, Y. Zhao, L. Miao, *J. Electrochem. Soc.* 159 (2012) A894.
- [31] A. Caballero, L. Hernan, M. Melero, J. Morales, R. Moreno, B. Ferrari, *J. Power Sources* 158 (2006) 583–590.
- [32] Y. Talyosef, B. Markovsky, G. Salitra, D. Aurbach, H.J. Kim, S. Choi, *J. Power Sources* 146 (2005) 664–669.
- [33] K.M. Shaju, P.G. Bruce, *Dalton Trans.* (2008) 5471–5475.
- [34] P.G. Bruce, B. Scrosati, J.M. Tarascon, *Angew. Chem. Int. Ed. Engl.* 47 (2008) 2930–2946.
- [35] Z. Chen, S. Qiu, Y. Cao, X. Ai, K. Xie, X. Hong, H. Yang, *J. Mater. Chem.* 22 (2012) 17768–17772.
- [36] D.I. Choi, H. Lee, D.J. Lee, K.-W. Nam, J.-S. Kim, R.A. Huggins, J.-K. Park, J.W. Choi, *J. Mater. Chem. A* 1 (2013) 5320–5325.
- [37] Y. Qian, Y. Deng, Z. Shi, Y. Zhou, Q. Zhuang, G. Chen, *Electrochim. Commun.* 27 (2013) 92–95.
- [38] Y.-G. Guo, J.-S. Hu, L.-J. Wan, *Adv. Mater.* 20 (2008) 2878–2887.
- [39] Y. Wang, H. Li, P. He, E. Hosono, H. Zhou, *Nanoscale* 2 (2010) 1294–1305.
- [40] J.C. Arrebola, A. Caballero, L. Hernan, J. Morales, *Electrochim. Solid-State Lett.* 8 (2005) A641.
- [41] S. Dalavi, M. Xu, B. Knight, B.L. Lucht, *Electrochim. Solid-State Lett.* 15 (2012) A28.
- [42] Y. Cui, X. Zhao, R. Guo, *J. Alloys Compd.* 490 (2010) 236–240.